

Article

Applicability of Earth Observation for Identifying Small-Scale Mining Footprints in a Wet Tropical Region

Celso M. Isidro ^{1,*}, Neil McIntyre ¹ , Alex M. Lechner ^{1,2}  and Ian Callow ^{1,3}

¹ Centre for Water in the Minerals Industry, Sustainable Minerals Institute, The University of Queensland, St. Lucia Campus, QLD 4072, Australia; n.mcintyre@uq.edu.au (N.M.);
Alex.Lechner@nottingham.edu.my (A.M.L.); i.callow@uq.edu.au (I.C.)

² School of Environmental and Geographical Sciences, Faculty of Science,
University of Nottingham Malaysia Campus, Jalan Broga, Semenyih 43500, Malaysia

³ Rio Tinto Limited, 123 Albert St., Brisbane, QLD 4000, Australia

* Correspondence: celso.isidro@uq.net.au; Tel.: +63-929-799-0217

Received: 22 August 2017; Accepted: 8 September 2017; Published: 12 September 2017

Abstract: The unpredictable climate in wet tropical regions along with the spatial resolution limitations of some satellite imageries make detecting and mapping artisanal and small-scale mining (ASM) challenging. The objective of this study was to test the utility of Pleiades and SPOT imagery with an object-based support vector machine (OB-SVM) classifier for the multi-temporal remote sensing of ASM and other land cover including a large-scale mine in the Didipio catchment in the Philippines. Historical spatial data on location and type of ASM mines were collected from the field and were utilized as training data for the OB-SVM classifier. The classification had an overall accuracy between 87% and 89% for the three different images—Pleiades-1A for the 2013 and 2014 images and SPOT-6 for the 2016 image. The main land use features, particularly the Didipio large-scale mine, were well identified by the OB-SVM classifier, however there were greater commission errors for the mapping of small-scale mines. The lack of consistency in their shape and their small area relative to pixel sizes meant they were often not distinguished from other land clearance types (i.e., open land). To accurately estimate the total area of each land cover class, we calculated bias-adjusted surface areas based on misclassification values. The analysis showed an increase in small-scale mining areas from 91,000 m²—or 0.2% of the total catchment area—in March 2013 to 121,000 m²—or 0.3%—in May 2014, and then a decrease to 39,000 m²—or 0.1%—in January 2016.

Keywords: artisanal and small-scale mining; geographic-object-based image analysis; wet tropical region; Philippines; Didipio catchment; object-based support vector machine

1. Introduction

Small-scale mines are defined as a mine that operates using rudimentary mining and milling methods (minimal mechanization and minimal, or absence of, structures that control mine and mill spillages) at the level of individuals, families or cooperatives, and temporarily makes a specific mining claim or in other cases may be illegal [1,2]. Small-scale mines can be major contributors to local economies and livelihoods [3,4] but in many cases, this comes with significant environmental impacts due to unsuitable locations, rudimentary mining methods, and lack of effective regulation [5,6]. The diffuse and remote locations of the mine sites—and their relatively short and unpredictable life span—impede the systematic documentation of small-scale mine development and footprints [7]. This is challenging for accurately surveying land use, the accurate attribution of impacts and the targeting of regulatory resources.

The difficulty of effectively monitoring small-scale mining using traditional surveys calls for supplementary approaches based on remote sensing. The application of remote sensing from satellites, in conjunction with supervised techniques for classifying land use and land cover (LULC), is attractive for several well-established reasons. Remote sensing provides the opportunity to observe changes in LULC over inaccessible regions. By combining images from different passes of one or more satellites, the evolution of LULC can be modelled. For example, Landsat now provides 45 years of historical records from 1972 [8]. Continual improvements in spatial, spectral, radiometric and temporal resolutions are permitting greater levels of information about the type, timing and extent of changes to be obtained.

Small-scale mining, however, introduces some challenges to applying remote sensing and associated land use classification techniques. The surface footprints for smaller mines may only be tens of meters, and less for underground mines or mines in early stages of development, reducing the applicability of Landsat and other freely accessible products with moderate spatial resolutions. Another challenge is that the visible footprint of the mines—mainly vegetation and top-soil clearance—is similar to many other land cover and land use changes such as clearance for agriculture or forestry and is thus likely to have similar spectral responses. Moreover, mining areas can be confused with recently burned forest [9]. Finally, small-scale mining is a dynamic land use and mines can be established and abandoned within a period of months therefore they may be difficult to capture with, bi-annual or annual images for example. These challenges are especially problematic in wet tropical regions, where cloud cover is likely to prevent the use of a large proportion of available images, and regular rainfall-driven land-slides may confound the identification of mines.

A key challenge for the remote sensing of mining land cover is that several forms of land use have similar spectral signatures [10]. Using pixel-based land cover classification approaches based only on differences in spectral signatures can therefore result in misclassifications. This can be exacerbated if the distributions of reflectance for each class are not normally distributed [11]. The limitations of pixel-based classification approaches have given rise to development of object-based segmentation techniques [12], which are collectively known as geographic-object-based image analysis (GEOBIA) [12,13]. Using GEOBIA, pixels with homogenous properties are merged to produce multiple segments (objects) where pixels are grouped based on not only their spectral properties but also the spatial and textural characteristics of the segments to which they potentially belong [13].

A recent advancement in GEOBIA classification methods has been the application of Support Vector Machines (SVM) to image objects instead of pixels using a technique known as object-based support vector machine (OB-SVM) [14]. Recent examples in the literature show that SVMs used with both pixels [13] and image objects [14,15] can outperform other classification algorithms (e.g., Decision Tree, Maximum Likelihood, Nearest Neighbor and Neural Networks). The SVM classifier is not based directly on differences between the statistical distribution of attributes of separate classes [15,16] but instead it uses non-parametric machine learning algorithms that determine the optimal boundaries among classes [11]. The SVM classifier is noteworthy for its ability to separate complex classes with limited training data [17]. In addition, the overall accuracy of an OB-SVM can be improved by including other spatial data such as Digital Elevation Model (DEM) and Vegetation Indices (VI) [14].

This research explored the utility of remote sensing for capturing land use change dynamics in wet tropical regions subject to transient small-scale mining using a case-study in the Didipio catchment region, Philippines. We applied the OB-SVM classifier to map land cover change for three different scenes between 2013 and 2016. Imagery was acquired from Pleiades-1A for the 2013 and 2014 scenes and from SPOT-6 for the 2016 scene. Historical spatial data on location and type of ASM mines were also collected from the field and were utilized as training data for the OB-SVM classifier. This was supplemented by manual image interpretation and ancillary spatial data for the other land covers in the region which included forests, rivers and the nearby Didipio large-scale mining operation. We conclude by discussing the utility of the methods and imagery in the context of the remote sensing of ASM in wet tropical regions.

2. Materials and Methods

2.1. Study Area

The Didipio catchment is situated in the Cagayan region of northeast Philippines. The anthropogenic land use features in this area include open land (deforested area), cultivated areas, small-scale gold mining and large-scale gold mining. Prior to this study, there was no publicly available documentation of land use in this region. Mining has become a principal land use since 2013, when operations started at the large-scale Didipio mine. This is composed of the open-pit mine and other mining structures such as haulage roads, stockpile areas and motor pool open wash bays with an estimated (as of January 2016) surface area of 2.23 km² (Figure 1). The mine expanded from phase 1 to phase 2 during the period between 2012 and 2013. The area has seven principal rivers of interest (Figure 1). The anthropogenic use of the Alimit, lower Didipio, Dupit and Surong rivers is primarily to support agriculture, whereas the Camgat, Camgat-Surong, Dinauyan and upper Didipio rivers are available for general community purposes but are also the focus of small-scale mining activity.

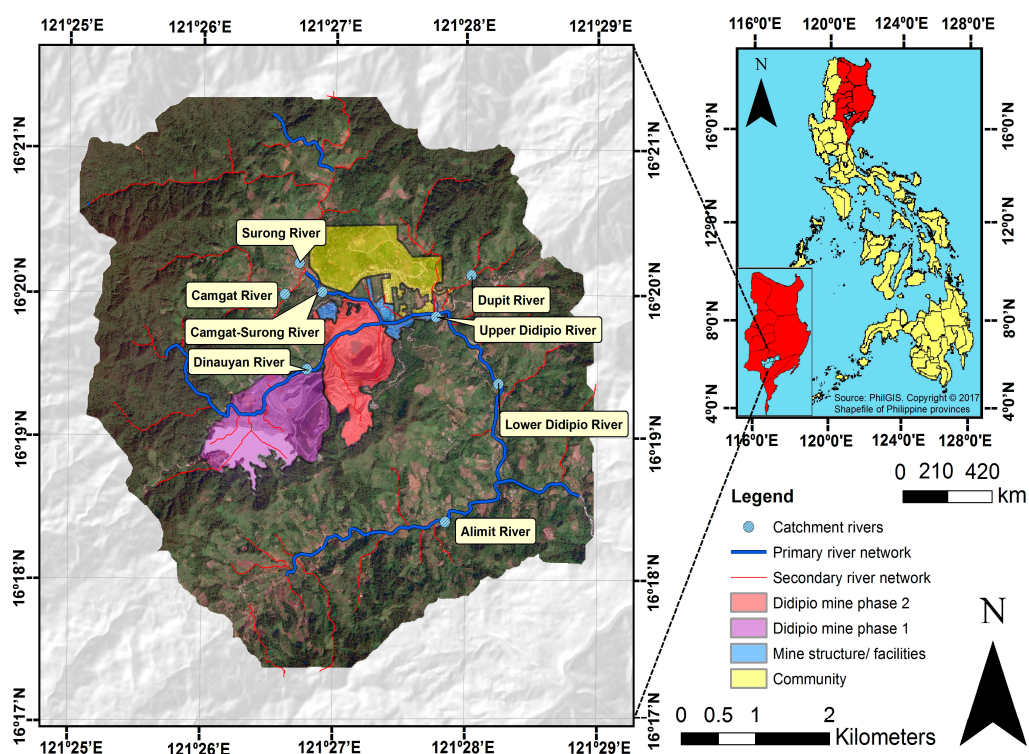


Figure 1. Major features of the Didipio catchment area in the Philippines. The land cover is shown only within the Didipio catchment area, while the extent of the figure corresponds to the boundary of the Pleiades-1A and SPOT-6 images.

On the other hand, the availability of cloud-free satellite data is generally only possible in the dry season between January and April, although a high percentage of cloud cover persists for most of that period. Landsat-8 Operational Land Imager (OLI), a satellite with a 16-day acquisition frequency, was tested for cloud-free image availability of the catchment between 2013 and 2016. Over the four years, only five to eight of its images were suitable for image analysis, while only two full images of delineated Didipio catchment were unobstructed by atmospheric effects. The remainder of the images are contaminated either by clouds, haze, or shadows.

Since 2012, the large-scale mine operator has kept a database of small-scale mine locations, based on ground surveys every three months. Each site is labelled as either an active or inactive mine. An inactive mine includes operational mines where there happened to be no activity on the

day of survey, as well as seemingly abandoned mines. Supplementary information, such as the mining technique and/or presence of processing equipment and earth-moving vehicles has also been recorded. This database was supplemented by ground surveys by the authors in November 2015 and February 2016. Figure 2 shows the evolution of the location and type of small-scale mines; and photographs for sample sites are presented in Figure 3.

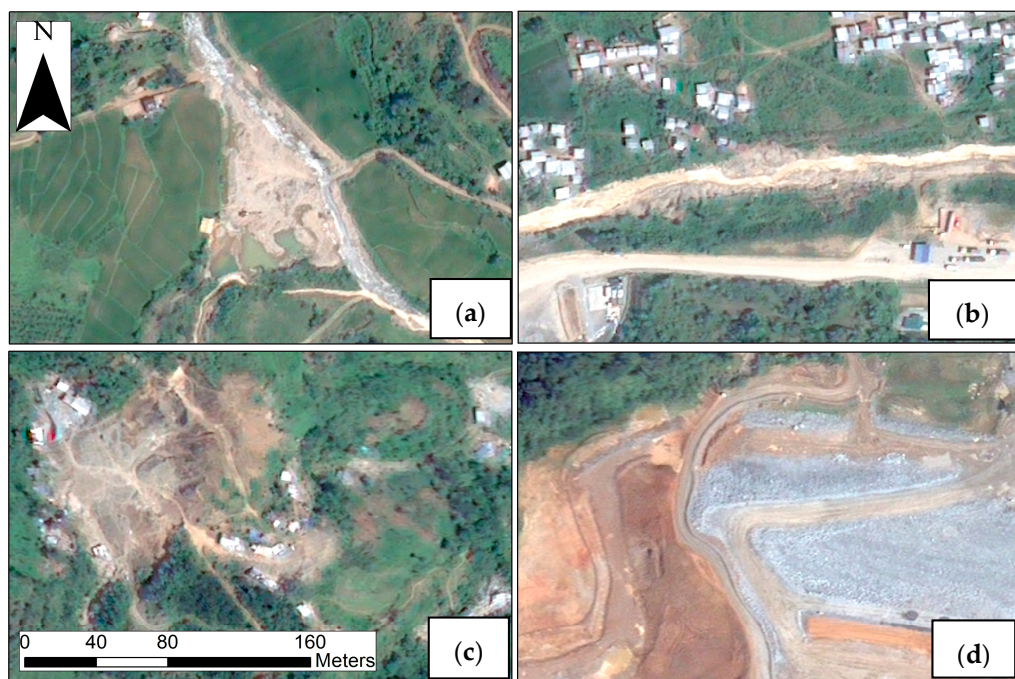


Figure 2. Different forms of mining in Didipio catchment: (a) Sediment pit; (b) Panning area; (c) Small-scale mines on hard rocks; (d) Large-scale open-pit mine.



Figure 3. Operating small-scale mines in Didipio catchment.

In March 2012, the majority of small-scale mining sites were near the rivers. During this period, excavating and panning the river sediments was the principal mining method (Figure 4). Out of the 43 panning sites, 26 were located in the upper and 8 in the lower Didipio River, while 9 were situated in smaller tributary creeks of the Dinauyan River (Figure 1). In addition, small-scale underground mining began to develop with tunnels operating perpendicular to these creeks, which became part of the Didipio mine phase 1 during the same year.

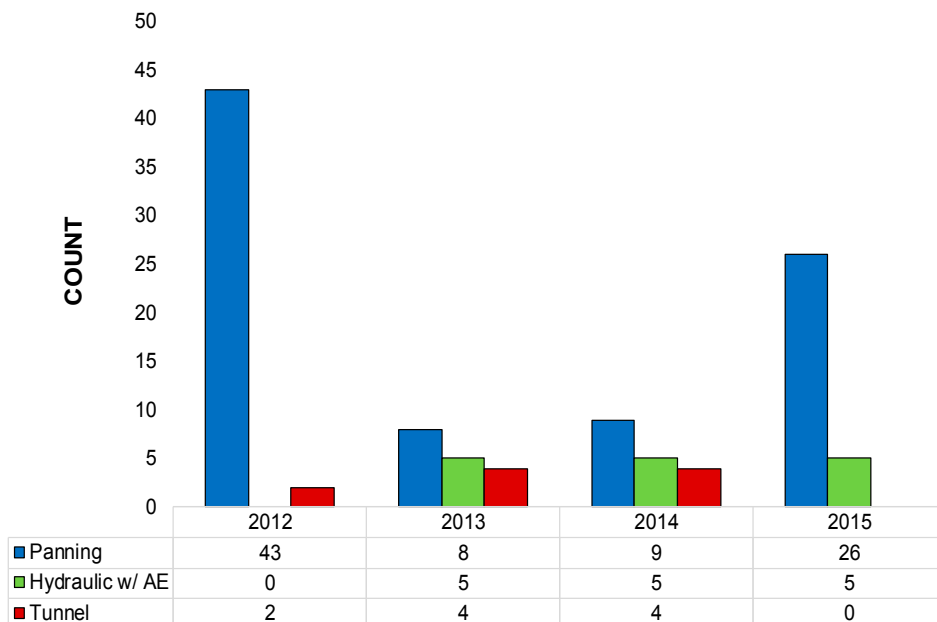


Figure 4. Active small-scale mining sites derived from field data from 2012 to 2015 categorized by mining method.

In 2013, hydraulic mining with assistance of hydraulic excavators was introduced in order to increase production yield. These mining practices became dominant in sites operating near the Dinauyan River and near the junction of the Camgat and Surong rivers. The development of small-scale underground mines remained common throughout 2013, with 4 newly constructed tunnels beside the lower Didipio River. All of the surveyed small-scale mines were between 50 and 100 m width in terms of land clearance and between 400 m² and 14,000 m² surface area. Those mines located on exposed rocks (left of lower Didipio River) appear similar to the open-pit mine in the images, whereas the mines near the rivers had a diverse appearance of sediments and topsoil (Figure 2).

By 2014, the majority of the small-scale mines had moved from their initial locations to higher elevations. Along the Camgat River, newly established larger scale mines (but still within the definition of small-scale mines) were observed. Meanwhile, the development of new underground mines slowed. In 2015, most of the mine tunnels had been abandoned but small-scale mines on the surface, particularly near the Camgat River, were still operating (Figure 5).

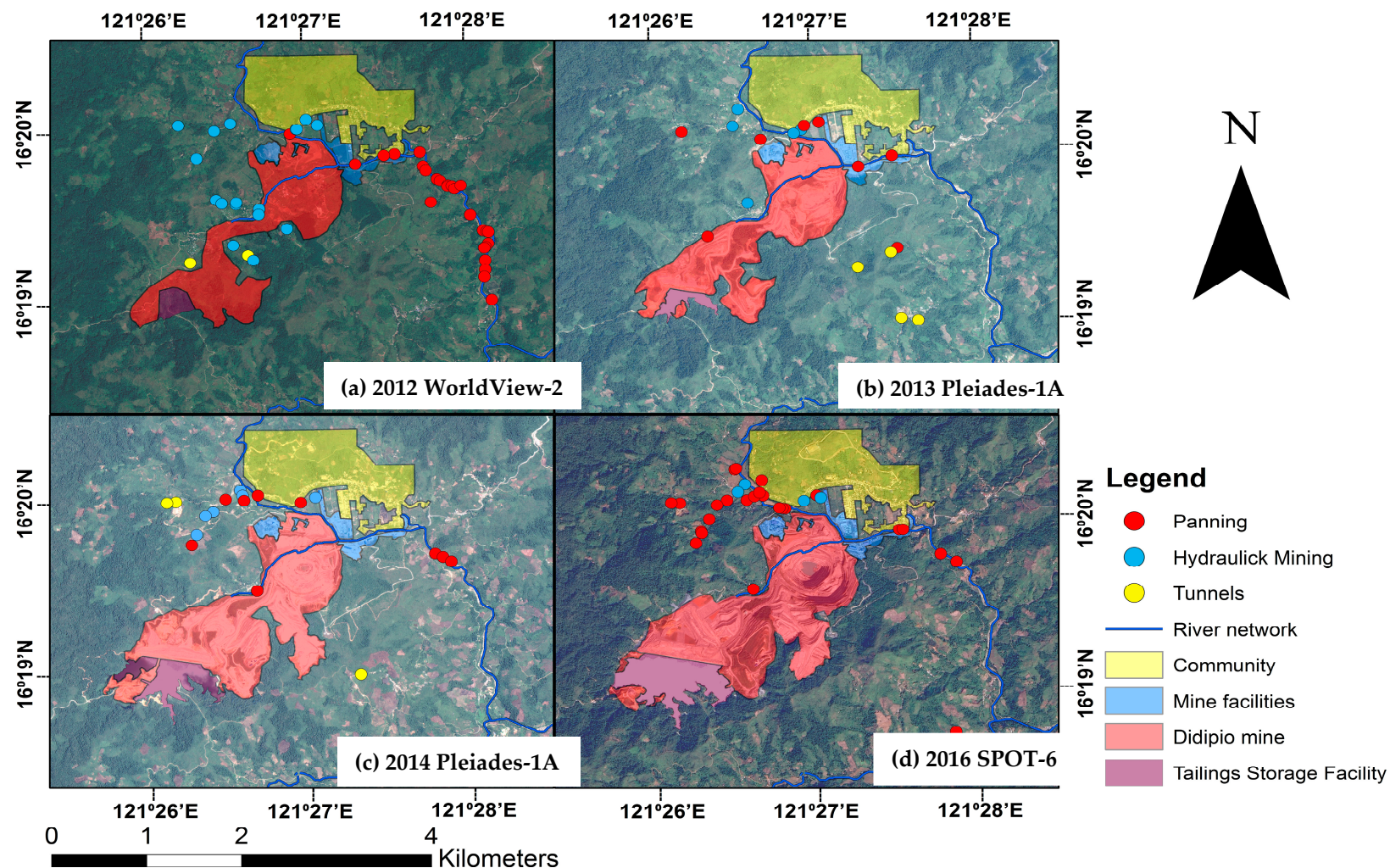


Figure 5. Locations and types of active small-scale mine sites based on ground surveys, superimposed on remote-sensed images. 2010 Satellite Image courtesy of the DigitalGlobe Foundation; Pleiades: © CNES (2013, 2014), Distribution Airbus DS/Spot Image; SPOT: © AIRBUS DS (2016). Note: 2010 data used due to lack of alternative cloud-free image in 2012.

2.2. Satellite Imagery

The size of small-scale mines was the primary consideration in selecting the source satellites with visible footprint widths as low as 50 m. Landsat 8 was discounted due to its low spatial resolution ($\sim 30 \times 30$ m pixel size). The availability of satellite images was also a limitation due to cloud cover. Two satellite data sources were selected, which addressed both these limitations—SPOT-6 and Pleiades-1A, with pixel sizes of 2 m and 6 m, respectively (Table 1).

Table 1. Acquisition dates and characteristics of the three scenes (2013, 2014, 2016) and corresponding sensor characteristics.

Satellite	Acquisition Date	Scene		Sensor				
		Sensor Angle (Degrees)	Cloud Cover (%)	Band	Designation	Wavelength (μm)	Spatial Resolution (m)	
Pleiades-1A	20 March 2013	23.74	1.2	1	Blue	0.43	—	0.55
	5 May 2014	4.89	1	2	Green	0.50	—	0.62
				3	Red	0.59	—	0.71
				4	Near-Infrared	0.74	—	0.94
				5	Panchromatic	0.47	—	0.83
SPOT-6	6 Jane 2016	11.93	2	1	Blue	0.46	—	0.53
				2	Green	0.53	—	0.59
				3	Red	0.63	—	0.70
				4	Near-Infrared	0.76	—	0.89
				5	Panchromatic	0.46	—	0.75
								1.5

The Pleiades and SPOT images originate from pairs of identical satellites (SPOT-6 and 7; and Pleiades-1A and 1B), which revolve in the same orbital plane [18], making it possible to secure coherent images with identical spatial extents every one to two days, increasing the probability of obtaining cloud-free images. In addition, both sources provide three spectral channels in the visible spectrum, a single channel of near-infrared and a panchromatic band. For the Didipio catchment, two images with near-zero cloud cover were captured by Pleiades-1A on 20 March 2013 and 5 May 2014, while one image with near-zero cloud cover was captured by SPOT-6 on 6 January 2016 (Table 1). Out of all the SPOT and Pleiades images from January 2012 to January 2016 with acceptable deviations from nadir, these images were the only ones identified with less than 2% cloud cover. Although images with more than 2% cloud coverage show some small-scale mining areas, the direct cloud areas combined with the cloud shadows were deemed to be too contaminating. Furthermore, the clouds tend to be at higher elevations and therefore the sampling errors introduced are not random. Likewise, Pleiades-1A and SPOT-6 images with low deviation of sensor angle from nadir (e.g., less than 25 degrees) were prioritized as they have less geometric errors to be corrected during orthorectification process [19,20].

2.3. Pre-Processing Stages of Satellite Image Data

2.3.1. Radiometric Calibration of Sensors

The radiometric calibration of the images was performed to: (1) normalize brightness values and (2) convert the data into Top-of-the-Atmosphere (ToA) reflectance. The calibration was conducted in two steps. The original geometrically corrected images provided by the supplier were calibrated to spectral radiance (L_λ) using (Equation (1)) [21–23] and gain and bias values obtained from the supplementary metadata for each acquisition. The output of Equation (1) for each image was used in Equation (2) to derive the ToA reflectance [21,22]. The band-specific exoatmospheric irradiance at a given sun elevation angle (θ_{SE}) and earth-sun distance (ESUN) during the acquisition of each image were also provided from the metadata. The earth-sun distances were manually calculated using

Equation (3) [24]. The Julian date in Equation (3) corresponds to the number of days between Universal time on 1 January 4713 BC and the capture time of the satellite image [25].

$$L_{\lambda} = \frac{Q_{\text{cal}}}{\text{GAIN}} + \text{BIAS} \quad (1)$$

$$P_{\lambda} = \frac{\pi \cdot L_{\lambda} \cdot d^2}{\text{ESUN} \cdot \cos(\theta_{\text{SZ}})} \quad (2)$$

$$d = 1 - 0.01672 \cos[0.9856(\text{JD} - 4)] \quad (3)$$

$$\theta_{\text{SZ}} = 90^{\circ} - \theta_{\text{SE}} \quad (4)$$

where L_{λ} = spectral radiance; Q_{cal} = Digital number; P_{λ} = ToA reflectance; ESUN = Solar irradiance; d = Earth-Sun distance; JD = Julian date; θ_{SZ} = Sun zenith angle; θ_{SE} = Sun elevation angle.

2.3.2. Atmospheric Correction

An atmospheric correction was then applied to the calibrated satellite images to reduce the effects of atmospheric absorption and scattering [24]. Atmospheric correction was applied using the Quick Atmospheric Correction (QUAC) algorithm provided in the ENVI software [26–28]. QUAC is an approximate, in-scene atmospheric approach that normalizes images based on the statistical properties of object spectra found within an image [29]. The QUAC algorithm can be applied when there are at least 10 diverse objects in the image [30]. The average reflectance of each object was used as a baseline reference. Prior to correction, objects with high reflectance values such as clouds were manually masked and highly structured regions in the image (e.g., forest areas) were selectively masked by the algorithm. This was followed by the linear transformation of spectral signatures by the QUAC algorithm through plotting their reflectance against a set of universal reference spectra of image objects (e.g., road networks, bare soil, river networks, roofs) from the software's spectral library [30]. The resulting outputs from the application of the atmospheric correction were surface reflectance values as opposed to the ToA reflectance values produced in the previous step.

2.3.3. Enhancement of Spatial Resolution through Image Fusion and Supplementary Pre-Processing Techniques

To increase the spatial resolution, image fusion with a pan-sharpening algorithm was applied to reduce the pixel size of the original multispectral images to that of the panchromatic band (0.50 m for Pleiades-1A and 1.5 m for SPOT-6). The nearest-neighbor diffuse (NND) algorithm was used from the ENVI software for this task. Unlike other pan-sharpening algorithms, this method processes spectral bands separately. NND operates on a per pixel basis, thus providing more accurate spectral information, which can improve land cover classification [31]. Furthermore, a mosaicing technique was applied to sections of the 2014 Pleiades-1A image with clouds over fixed land covers (e.g., forest). This section of the reference image had been clipped, and the reference image was merged with the cloud-free equivalent of this section from the 2013 Pleiades-1A image. For the concluding steps, a bilinear resampling technique was used for all the images. The spatial resolution of the Pleiades-1A images was reduced to 1 m to remove pixel noise and to increase the classification processing speed. In contrast, the pansharpened SPOT-6 image (1.5 m) was also resampled to 1 m. To smoothen the intensity contrast of image object boundaries, a 3×3 pixels median kernel was applied for all the satellite images. The final products were satellite images with 1 m spatial resolutions.

2.4. Classification Method

For the image classification, a two-step process was used (Figure 6). The example-based feature extraction workflow by ENVI was used for the application of OB-SVM, with segmentation parameters developed for each image. In the first step, each image was segmented. The scale of segmentation

was configured using the edge algorithm. This algorithm locates the outermost edge between image objects, which corresponds to adjacent pixels with the highest intensity contrast [32]. The segmentation work flow first creates small objects/segments which are then combined through the application of the full lambda schedule algorithm, which merges objects based on similarity of their spatial and spectral properties [33]. Before segmentation, a kernel size of 19 by 19 pixels was configured to calculate the values of the textural attributes of the segments. Since the pixel size of the final image is 1 m, the kernel resembles a 19×19 m box or 361 m^2 . This kernel size is sufficient to capture the textural difference (e.g., footprints) of small-scale mines from other land clearances. Although the segmentation parameters were configured in similar ways for all images, the SPOT-6 image had larger and fewer segments than Pleiades-1A due to the difference in spatial resolution between these two satellite sensors.

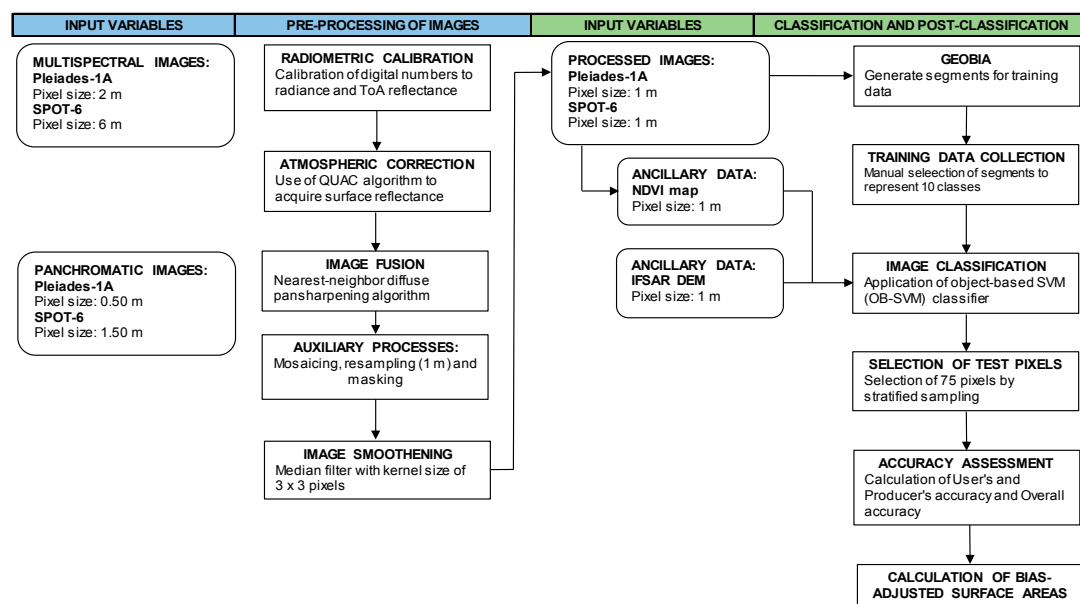


Figure 6. Flowchart of image pre-processing and image analysis (classification and post-classification).

After image segmentation, a proportion of segments were manually selected and classified to create training data for OB-SVM (Table 2). We classified 10 land cover types ranging from forest to small-scale mining. The classification was based on the baseline land cover map developed from the ecological assessment of the Didipio Project, the small-scale mining ground-truthing and manual interpretation of the images. Table 2 describes the number of training segments for each land cover type. Approximately 8% and 10% of the catchment areas were used as training data for the Pleiades-1A and SPOT-6 images, respectively. Due to differences in segment/object sizes for the SPOT-6 image, a lower number of segments was used as training however the total training area was larger at 10% of the catchment. There were also differences in the number of segments used for training data between land cover types. For example, as there are several forms of tree canopies present in the catchment, small segments were generated for forest classes and thus more segments were assigned. In addition, general expansion of various forms of land clearance (e.g., open land, large-scale mine) as well as the tailings storage facility were observed in the 2014 image, therefore more segments were selected to represent these land cover types in the training data. For the small-scale mine (SSM) class, the ground surveys that best coincided with the image acquisition dates were used to develop training data.

Table 2. Descriptions of the land use and land cover classes and size of training data in each image.

Classes	Training Data						Description	
	2013		2014		2016			
	Segment	Coverage (% of Catchment)	Segment	Coverage (% of Catchment)	Segment	Coverage (% of Catchment)		
Forest	1131	1.37	1156	1.88	491	2.15	Includes all types of trees in the catchment	
Grassland	463	2.71	267	1.71	252	2.40	Vegetated areas that do not contain any trees or shrubs	
Cultivated area	228	0.88	224	0.88	212	1.41	Agricultural lands	
Open land	186	0.81	382	1.60	214	1.57	Mixture of trees, shrubs, and newly burned/ cut forest timbers	
Large-scale mine	399	1.52	813	1.35	188	1.81	Open-pit mine and other natural mine components such as haulage roads, stockpile areas and motor pool open wash bays	
Tailings Storage Facility	13	0.05	40	0.36	25	0.04	Mine tailings dam	
Small-scale mine (SSM)	108	0.13	405	0.19	47	0.16	Includes all possible active mine sites in use for hydraulic mining, gold panning, and underground mining and improvised rough roads within the SSM	
Road system/Vacant lot	412	0.38	822	0.38	293	0.46	Includes the municipal road, access areas and vacant lots surrounding each house in the local community, access to mine facilities and camp site	
Built-up	171	0.05	229	0.09	214	0.09	House, buildings, and mineral processing facilities	
Stream network	226	0.15	157	0.11	69	0.14	Clear water, highly turbid water and riverbanks	
TOTAL	3337	8.05	4495	8.56	2005	10.23		

The OB-SVM classifier was then applied to the three scenes and ancillary data using the training data described above. Ancillary data in the form of Interferometric Synthetic Aperture Radar (IFSAR) Digital Elevation Model (DEM) with a vertical resolution of 5 m (resampled to 1 m) and NDVI calculated from the satellite imagery were used. The IFSAR DEM of the catchment was acquired between March and July 2013. Mine pits may be detected through DEMs of sufficient vertical resolution. This may aid the OB-SVM classifier to delineate mining areas from adjacent land covers (e.g., grassland), which have lower and more regular slopes. The DEM was used to form a composite image with the four spectral channels of each image and their respective NDVI maps through image stacking. These multiple spatial data were used as inputs for the calculation of the spatial, spectral and textural attributes of training data. The training data were used by the OB-SVM classifier to generate the thematic map of land use classes.

In the application of an OB-SVM, a range of kernels can be used for separating classes. Known kernels commonly used in remote sensing are polynomial and radial basis functions kernels, which perform well for classes that are nonlinearly separable [11]. For this research, a nonlinear radial basis function kernel of gamma (γ) = 0.01 was used for the Pleiades-1A image in 2013 based on previous literature and testing. For example, Huang et al. [11] tested values of γ from 0.1 to 1 and found γ = 0.1 gave the optimum boundaries among classes with less misclassification rate, whereas γ = 0.01 was used by Lin et al. [15] in classifying 10 LULC features. However, a γ of 0.05 was selected for the 2014 Pleiades-1A and 2016 SPOT-6, as our testing found it to have the best result for these images.

2.5. Accuracy Assessment

Seventy-five test pixels for each LULC class were sampled from the map of classification results and compared with the same pixels from the baseline assessment map. Stratified sampling was used, as implemented in the ENVI software. This sample size meets the guidelines provided from previous studies [34,35]. The training data pixels were excluded during sampling of test pixels. Correct and incorrectly classified pixels were used to generate a confusion matrix for each image. The Overall Accuracy of classification of each image (Equation (5)), Producer's Accuracy (error of omission; Equation (6)) and User's Accuracy (error of commission; Equation (7)) were then calculated [35].

$$OA = \frac{\sum_{i=1}^n R_i}{\sum_{i=1}^n N_i} \quad (5)$$

$$PA_i = \frac{R_i}{M_i} \quad (6)$$

$$UA_i = \frac{R_i}{N_i} \quad (7)$$

where OA = Overall accuracy; PA = producer's accuracy; UA = User's accuracy; n = Number of classes; R_i = Number of correctly classified test pixels in class i; N_i = Number of test pixels that are classified to be in class i (=75); M_i = Number of test pixels that are in class i in the baseline map.

We also assessed biases in classification. For each class j, the proportion of the total catchment area wrongly classified as i was estimated as P_{ij} (Equation (8)). These proportions were used to adjust the original classification results (A_{Total}) to give an improved estimate of the actual surface area for this class (A_j) (Equation (9)) [36]. The standard error for the proportion of each class was determined (Equation (10)) to generate the specific standard error of every bias-adjusted surface area (Equation (11)). Furthermore, to obtain the margin of error of a class, the standard error of a bias-adjusted surface area is multiplied by the z-score of the standard distribution at 95% confidence that is 1.96 or simply equivalent to two.

$$P_{ij} = W_i \cdot \frac{t_{ij}}{t_i} \quad (8)$$

$$A_j = A_{Total} \cdot \sum_i P_{ij} \quad (9)$$

$$S(P_j) = \sqrt{\sum_{i=1}^n W_i^2 \frac{\frac{t_{ij}}{t_i} (1 - \frac{t_{ij}}{t_i})}{t_i - 1}} \quad (10)$$

$$S(A_j) = S(P_j) \cdot A_{\text{Total}} \quad (11)$$

where P_{ij} = weight of misclassified test pixels in each row; t_{ij} = number of misclassified test pixels in each column; t_i = number of assigned test pixels in each row; W_i = ratio of the calculated class area and total catchment area; A_j = Bias-adjusted surface area; $S(P_j)$ = Standard error.

3. Results and Discussion

3.1. Comparison of Spectral Signatures across LULC Classes

Comparing the spectral signatures for the training data (Figure 7) gives some insight into the challenge of classification. Unlike the vegetated areas (e.g., forest, grassland, cultivated area), which have distinct reflectance values in the near infrared channel (825 nm), several classes (Figure 7 Plot 1B, 2B, 3B) in which soil is exposed have similar reflectance across all spectral channels. These classes include: open land made up of stripping and burning of vegetation; small-scale mines in which deeper soil layers were brought to the surface; roads mainly made up of compacted sand and gravel; and the mine pit benches. Adding to the challenges, the stream network comprises of clear water, highly turbid water and riverbanks, and results in a spectral signature similar to the forms of bare soil. The application of NDVI maps helped separate vegetated areas from bare soil and the variation of reflectance in the near infrared region provides some information on the potential presence of patches of vegetation. For instance, the open land in the 2013 image, despite having the lowest overall reflectance in the visible spectrum, has the highest surface reflectance in the near infrared channel. However, this was unhelpful for distinguishing small-scale mines from other forms of bare soil.

The results in Figure 7, therefore, illustrate that the differences in spectral signatures are small between several classes of land and spectral attributes alone are unlikely to be sufficient to separate the small-scale mines from other LULC classes that are or appear to be stripped land. This illustrates the importance of GEOBIA, which also considers the spatial and textural properties of image objects.

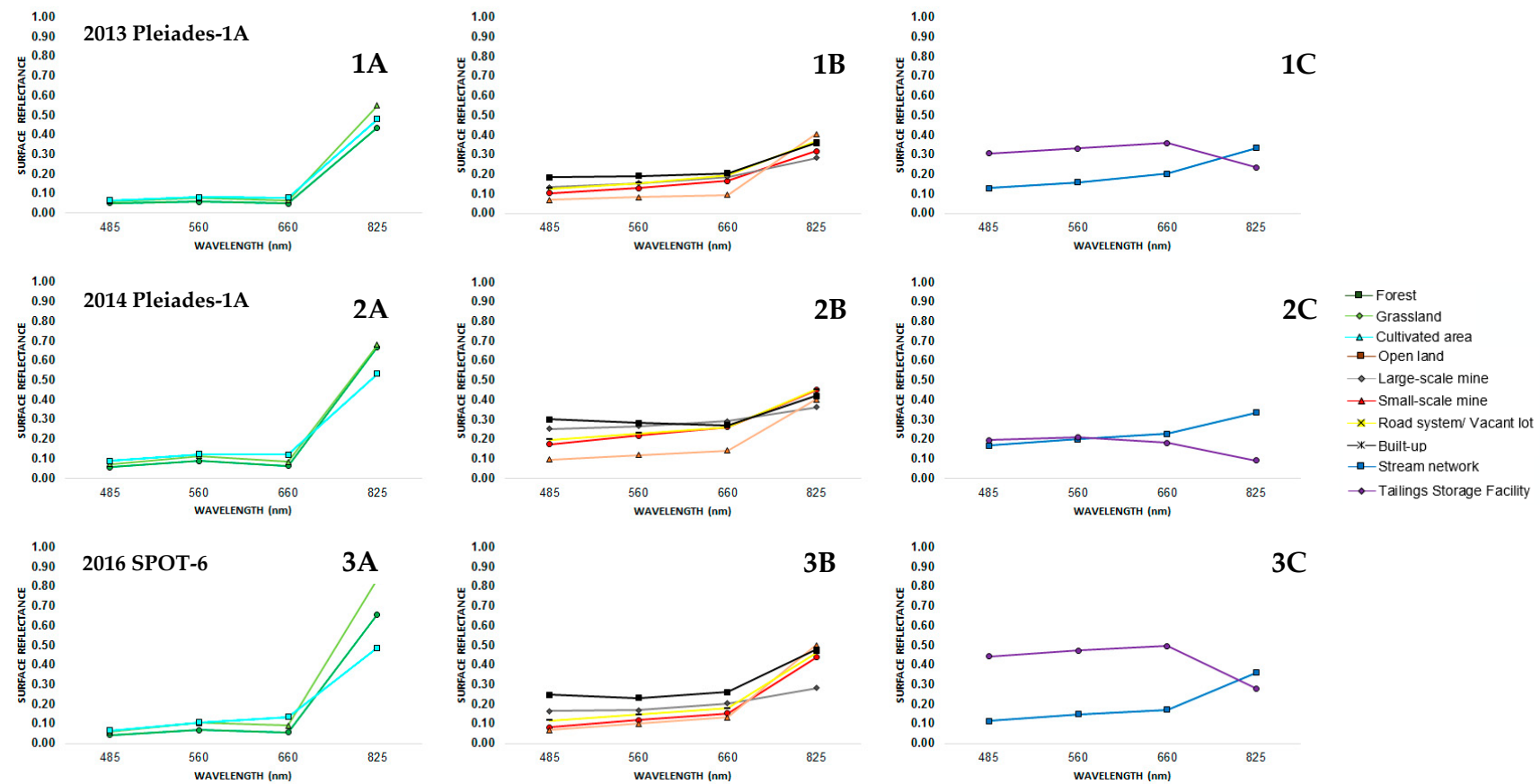


Figure 7. Plots with suffixes A, B and C describe variation in spectral signatures of vegetated areas, stripped lands and water bodies, respectively, from the three different images where prefixes 1, 2 and 3 correspond to 2013 Pleiades-1A, 2014 Pleiades-1A and 2016 SPOT-6 images.

3.2. Accuracy Assessment of Classification for Pleiades-1A and SPOT-6 Images

The application of the Pleiades-1A and SPOT-6 images and the OB-SVM classifier to locate small-scale mines had acceptable performance in terms of the Producer's Accuracy (PA) values. The PA values for the SSM class were 90%, 93% and 96% for the 2013, 2014 and 2016 images, respectively (Table 3). The high PA values illustrate that almost all of the small-scale mines were correctly classified. However, lower values of User's Accuracy (UA) were obtained for the SSM class: 76%, 69% and 69% for the 2013, 2014 and 2016 images, respectively (Table 3). The lower UA values illustrate that a significant number of pixels were misclassified as SSM. This was due to the pixels classified as SSM which included irregular segments of vacant house lots, large-scale mining, cultivated areas and open land. Still, the overall accuracy of the OB-SVM classifier applied to these images can be considered satisfactory, with OA values of 89%, 87% and 89% for the 2013, 2014 and 2016 images, respectively.

The misclassification of other LULCs as SSM may be attributed to several factors. Firstly, Table 3 shows that 4% to 13% of test pixels in the 2013, 2014 and 2016 images that were actually large-scale mining were misclassified as SSM. This is likely to be due to spectral and textural similarities of the SSM class with the construction of the in-pit ramps and benches between 2013 and 2016. The application of the IFSAR DEM as ancillary data during image classification only contributed in discriminating the sections of large-scale mine that were already present at the time of acquisition of the IFSAR DEM. The IFSAR DEM provided the information on the ground depression difference between the large-scale mine and the small-scale mines as well as their distribution throughout the catchment. The large-scale open pit mine was also among the well-classified LULCs, with UA values of 95%, 97% and 100%. Its size, unique shape and textural consistency generated distinguishable segments that were easily recognized by the OB-SVM classifier.

Moreover, in the 2013 and 2016 images, 8% of the cultivated area test pixels were misclassified as SSM. In SSM, stripping of ground cover is selective, and difficult-to-access ore bodies are left partially stripped and less undisturbed. On several occasions, the extraction of only a single section of the ore was observed over an extended period. Therefore, although deeper soil layers are exposed, these areas are often appearing as superficial disturbance that is easily misclassified as cultivated area or open land. In addition, both SSM and open land classes include irregularly shape segments. This kind of misclassification was also encountered in 2014 image, but with lower frequency. This is likely to be because the higher spatial resolution of this image allowed the textural features of small-scale mines to be better distinguished.

The resulting UA for the SSM class may be improved if sufficient cloud-free images could be obtained to capture the growing season, when cultivated areas and open lands have minimal stripping activities and therefore are less likely to be misclassified as SSM. The efficacy of the OB-SVM classifier may be examined in other catchments less affected by cloud cover. In addition, the Didipio catchment was challenging due to presence of several types of SSM with limited coverage.

Table 3. Generated Confusion Matrix for each image: (a) 2013 Pleiades-1A; (b) 2014 Pleiades-1A; (c) 2016 SPOT-6. (F: Forest, GL: Grassland, CA: Cultivated area, OL: Open land, LSM: Large-scale mine, TSF: Tailings Storage Facility, SSM: Small-scale mine, RS: Road system/Vacant lot, BU: Built-up, SN: Stream network, PA: Producer's accuracy, UA: User's accuracy).

(a) 2013 Pleiades-A		Ground Truth Classification										Total	UA (%)
		F	GL	CA	OL	LSM	TSF	SSM	RS	BU	SN		
OB-SVM CLASSIFICATION	F	75	0	0	0	0	0	0	0	0	0	75	100
	GL	4	68	3	0	0	0	0	0	0	0	75	91
	CA	4	14	55	2	0	0	0	0	0	0	75	73
	OL	1	0	2	72	0	0	0	0	0	0	75	96
	LSM	0	0	1	0	71	0	0	3	0	0	75	95
	TSF	0	0	0	0	0	75	0	0	0	0	75	100
	SSM	0	1	6	2	3	0	57	6	0	0	75	76
	RS	0	0	0	0	6	0	5	59	0	5	75	79
	BU	0	0	0	0	0	0	0	0	73	2	75	97
	SN	0	0	4	0	0	0	1	11	0	59	75	79
TOTAL		84	83	71	76	80	75	63	79	73	66	750	
PA (%)		89	82	77	95	89	100	90	75	100	89		
(b) 2014 Pleiades-1A		Ground Truth Classification										Total	UA (%)
		F	GL	CA	OL	LSM	TSF	SSM	RS	BU	SN		
OB-SVM CLASSIFICATION	F	74	1	0	0	0	0	0	0	0	0	75	99
	GL	2	71	2	0	0	0	0	0	0	0	75	95
	CA	0	16	52	5	0	0	0	2	0	0	75	69
	OL	1	1	4	66	2	0	0	1	0	0	75	88
	LSM	0	0	0	0	73	0	1	1	0	0	75	97
	TSF	0	0	0	0	6	69	0	0	0	0	75	92
	SSM	0	0	2	5	5	0	52	11	0	0	75	69
	RS	0	0	2	1	9	0	3	60	0	0	75	80
	BU	0	0	0	0	1	0	0	0	74	0	75	99
	SN	2	0	4	7	0	0	0	4	0	58	75	77
TOTAL		79	89	66	84	96	69	56	79	74	58	750	
PA (%)		94	80	79	79	76	100	93	76	100	100		

Table 3. *Cont.*

(c) 2016 SPOT-6	Ground Truth Classification										Total	UA (%)
	F	GL	CA	OL	LSM	TSF	SSM	RS	BU	SN		
OB-SVM CLASSIFICATION	F	75	0	0	0	0	0	0	0	0	75	100
	GL	5	70	0	0	0	0	0	0	0	75	93
	CA	2	2	57	9	0	0	1	4	0	75	76
	OL	0	1	2	66	2	0	0	4	0	75	88
	LSM	0	0	0	0	75	0	0	0	0	75	100
	TSF	0	0	0	0	2	73	0	0	0	75	97
	SSM	0	0	6	0	10	0	52	7	0	75	69
	RS	0	0	1	1	10	0	1	59	0	3	75
	BU	0	0	0	0	2	0	0	0	73	0	75
	SN	0	0	0	0	0	0	0	4	0	71	95
TOTAL		82	73	66	76	101	73	54	78	73	74	750
PA (%)		91	96	86	87	74	100	96	76	100	96	

3.3. Coverage and Spatial Distribution of Areas Classed as SSM Relative to other LULC Classes

The spatial distribution of the ten LULC classes is presented in Figure 8 with areas listed in Table 4. Although there are misclassifications among the classes (Table 4)—if it is assumed that biases identified for the test pixels represent the whole catchment—these classified areas can be bias-adjusted with given margins of error (Table 4) [36]. The areas referred to in the discussion below are the bias-adjusted values. Forest was the dominant natural landscape and, according to the OB-SVM classifier, it occupied 60% of the total catchment on average over the three years, mostly in the outer, higher altitude regions of the catchment. Meanwhile, grasslands were classified as being the next most dominant, representing an average of 23% of the area, concentrated at lower altitudes surrounding the large-scale mine. For stripped areas, the dominant LULCs according to the classifier were open land, large-scale mining and the road system/vacant lots, with average areas of 1.94, 1.95 and 0.68 km². The cultivated areas were constant at approximately 1.3 km². The area classified as SSM was on average 0.098 km² representing only 0.25% of the total catchment area, the smallest LULC footprint among the ten LULC classes. However, the small-scale mining activity may involve, as well as the mines themselves, LULCs included under the open land, road system/vacant lot classes.

Over the three years, there were significant changes in the mining activity. The areas classified as large-scale mine and the tailings storage facility (TSF) increased by 0.77 km² and 0.36 km², respectively. The area classified as SSM increased slightly from 0.091 to 0.121 km² between the 2013 and 2014 images. However, there was a decrease in 2016 by 0.039 km². Based on that result, the estimated area coverages of SSM were 0.091 km², 0.121 km² and 0.082 km² for the 2013, 2014 and 2016 images. The decline in small-scale mining in the 2016 image is counter-intuitive if it is considered that all abandoned mines should be classed as SSM. However, abandoned mines that have revegetated were not included in the ground truth surveys, and if they were included in the training data, they will be recognized under other classes. Uncertainty in the change in SSM coverage, based on the estimated margin of errors (Table 4), is relatively high and it is possible that the change from 2013 to 2014 is an artefact of misclassification errors. If it is real, this temporal change in SSM class coverage can be said to be significant at local scale only.

The generated thematic maps, apart from evaluating the SSM coverage, show how sediment pits and panning areas are more likely to develop once active whereas underground mines have more static footprints. In addition, these maps also permit judgment about the type of small-scale mining and how it varies throughout the catchment. For instance, the proximity to a river of areas classed as SSM as well as the presence of small ponds within these areas indicate sediment pits (Figure 5). From this, it is inferred that the small-scale mines neighboring the Camgat River, and those situated north of Camgat-Surong River besides the mine facilities/camp site are mostly sediment pits. This is supported by the ground surveys, where pumps and pipes were observed in these areas. Areas in the upper and lower Didipio River that were classified as SSM were identified in the ground surveys as well as in the images as scoured river banks associated with panning. In contrast, areas classed as SSM to the south of the upper Didipio River (Figure 2c), which were ground-truthed as tunnels, are almost 800 m away from the nearest river, and a decreasing surface area was observed within three years. Despite the identified dynamics, overall the areas classified as SSM remained in the same parts of the catchment. It may be concluded that high resolution satellite images may be useful, not only for identifying areas that are likely to include small-scale mines, but also for distinguishing between the main types of small-scale mine.

Table 4. Classified areas and Bias-adjusted areas of each LULC class.

Land Use and Land Cover Features	2013			2014			2015		
	Classified Area (km ²)	Bias-Adjusted Area (km ²)	Margin of Error (\pm km ²)	Classified Area (km ²)	Bias-Adjusted Area (km ²)	Margin of Error (\pm km ²)	Classified Area (km ²)	Bias-Adjusted Area (km ²)	Margin of Error (\pm km ²)
Forest	24.29	24.91	0.53	22.33	22.31	0.69	23.13	23.80	0.56
Grassland	10.13	9.40	0.69	8.82	8.95	0.77	9.54	8.96	0.56
Cultivated area	1.12	1.29	0.48	1.23	1.30	0.40	1.26	1.02	0.07
Open land	1.13	1.12	0.07	3.31	3.03	0.26	1.70	1.65	0.13
Large-scale mine	1.49	1.46	0.09	2.01	2.17	0.16	2.06	2.23	0.09
Tailings Storage Facility	0.07	0.07	0	0.26	0.24	0.02	0.45	0.43	0.02
Small-scale mine	0.07	0.09	0.03	0.09	0.12	0.07	0.08	0.08	0.02
Road system/Vacant lot	0.58	0.55	0.09	0.80	0.77	0.14	0.70	0.72	0.11
Built-up	0.17	0.17	0.01	0.18	0.18	0.01	0.18	0.18	0.01
Stream network	0.20	0.20	0.04	0.22	0.17	0.02	0.15	0.17	0.03
TOTAL	39.25	39.25		39.25	39.25		39.25	39.25	

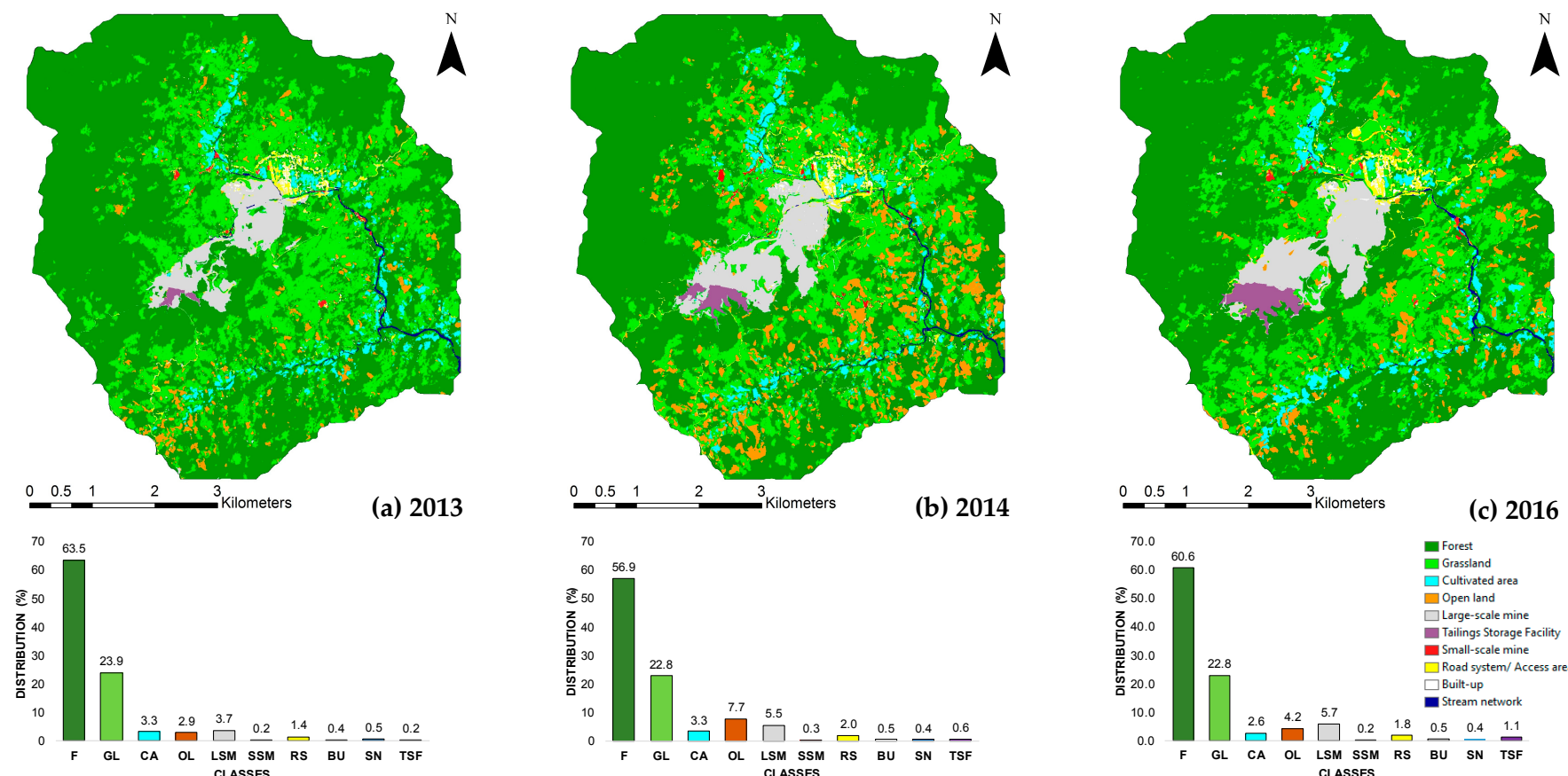


Figure 8. Output thematic maps and the corresponding land use class coverage distributions: (a) 20 March 2013 Pleiades-1A; (b) 5 May 2014 Pleiades-1A; (c) 6 January 2016 SPOT-6.

4. Conclusions

Small-scale mining often occurs in remote regions, and may occupy smaller areas and be more transient than other economic LULCs. It is therefore often challenging to identify and regulate effectively. The increasing availability of high resolution satellite images is potentially applicable to automatic mapping of small-scale mining development. However, the availability of cloud-free images and the presence of different types of LULCs that involve stripping vegetation and soil may create challenges, especially in wet tropical regions. This work has explored these challenges by applying high resolution images to mapping small-scale mining over three years in the Didipio catchment in the north-east Philippines.

The application of the OB-SVM to selected Pleiades-1A and SPOT-6 images produced thematic LULCs maps with an overall accuracy between 87% and 89%. The small-scale mining class was one of the least reliably identified, with user accuracy values from 69 to 76% and producer accuracy values from 90 to 96%. The common misclassification of other LULC classes as small-scale mining arose from the spatial, spectral and textural similarities of various forms of bare soil. In contrast, the more unique shape and topographical features of the large-scale mine meant that it was more reliably classified, with user and producer accuracy values ranging from 95 to 100% and 74 to 89%, respectively. Including the textural attributes was essential in determining the footprints of small-scale mines, for which high-resolution images of at least 1.5 m are probably essential.

Qualitative inspection of the thematic maps produced by the high-resolution images also indicated that it may be possible to estimate the type of small-scale mine by the spatial and temporal context. The primary limitation of this research was the low availability of suitable satellite images due to the regular cloud-cover over the catchment. Increasing frequency of images may in future permit larger training data sets and further improvements in reliably tracking the development of small-scale mines.

Acknowledgments: This research was prepared in part through the funding provided by the Australia Awards Scholarship and Sustainable Minerals Institute Research Support. In addition, the authors would like to acknowledge OceanaGold (Philippines) Incorporated Environmental Team, International River Foundation (IRF) and Mines and Geosciences Bureau (MGB), Region II for the permission to access their water quality data as well as providing technical assistance during ground works; the DigitalGlobe Foundation for the provision of a 2010 WorldView-2 image of Didipio catchment in support of the research; the National Mapping and Resource Information Authority (NAMRIA) in the Philippines for the provision of IFSAR DEM and Airbus Defence and Space for the acquisition of Pleiades-1A satellite images in 2013 and 2014 and SPOT-6 in 2016.

Author Contributions: Celso M. Isidro and Ian Callow designed the project; Celso M. Isidro performed the analysis and lead the writing of the paper; Neil McIntyre and Alex M. Lechner provided advice on the analysis and contributed to writing of the paper.

Conflicts of Interest: The authors declare no conflict of interest. The founding sponsors had no role in the design of the study; in the collection, analyses, or interpretation of data; in the writing of the manuscript, and in the decision to publish the results.

References

1. Hentschel, T.; Hruschka, F.; Priester, M. *Global Report on Artisanal & Small-Scale Mining*; International Institute for Environment and Development: London, UK, 2002; pp. 3–64.
2. Sousa, R.; Veiga, M.; Meech, J.; Jokinen, J.; Sousa, A. A Simplified Matrix of Environmental Impacts to Support an Intervention Program in a Small-Scale Mining Site. *J Clean Prod.* **2011**, *19*, 580–587. [[CrossRef](#)]
3. Labonne, B. Commentary: Harnessing Mining for Poverty Reduction, Especially in Africa. *Nat. Resour. Forum* **2002**, *26*, 69–73. [[CrossRef](#)]
4. Hilson, G. *The Socio-Economic Impacts of Artisanal and Small-Scale Mining in Developing Countries*; Taylor & Francis: Lisse, The Netherlands, 2003; ISBN 978-0-203-97128-4.
5. Cordy, P.; Veiga, M.; Salih, I.; Al-Saadi, S.S.; Garcia, O.; Mesa, L.A.; Velasquez-Lopez, P.; Roeser, M. Mercury Contamination from Artisanal Gold Mining in Antioquia, Colombia: The World's Highest per Capita Mercury Pollution. *Sci. Total Environ.* **2011**, *410–411*, 154–160. [[CrossRef](#)] [[PubMed](#)]

6. McIntyre, N.; Bulovic, N.; Cane, I.; McKenna, P. A Multi-Disciplinary Approach to Understanding the Impacts of Mines on Traditional Uses of Water in Northern Mongolia. *Sci. Total Environ.* **2016**, *404–414*, 557–558. [[CrossRef](#)] [[PubMed](#)]
7. Telmer, K.; Stapper, D. *Evaluating and Monitoring Small Scale Gold Mining and Mercury Use: Building a Knowledge-Base with Satellite Imagery and Field Work*; Aqueous Geochemistry Laboratory, School of Earth and Ocean Sciences, University of Victoria: Victoria, Canada, 2007; pp. 1–48.
8. Goward, S.; Masek, J.; Williams, D.; Irons, J.; Thompson, R.J. The Landsat 7 Mission: Terrestrial Research and Applications for the 21st Century. *Remote Sens. Environ.* **2001**, *78*, 3–12. [[CrossRef](#)]
9. Luethje, F.; Kranz, O.; Schoepfer, E. Geographic Object-Based Image Analysis Using Optical Satellite Imagery and GIS Data for the Detection of Mining Sites in the Democratic Republic of Congo. *Remote Sens.* **2014**, *6*, 6636–6661. [[CrossRef](#)]
10. Myint, S.; Gober, P.; Brazel, A.; Grossman-Clarke, S.; Weng, Q. Per-Pixel vs. Object-Based Classification of Urban Land Cover Extraction Using High Spatial Resolution Imagery. *Remote Sens. Environ.* **2011**, *115*, 1145–1161. [[CrossRef](#)]
11. Huang, C.; Davis, L.S.; Townshend, J.R.G. An Assessment of Support Vector Machine for Land Cover Classification. *Int. J. Remote Sens.* **2002**, *23*, 725–749. [[CrossRef](#)]
12. Blaschke, T. Object Based Image Analysis for Remote Sensing. *ISPRS J. Photogramm. Remote Sens.* **2010**, *65*, 2–16. [[CrossRef](#)]
13. Tzotsos, A.; Argialas, D. Support Vector Machine Classification for Object-Based Image Analysis. In *Object-Based Image Analysis*; Springer: Heidelberg / Berlin, Germany, 2008; pp. 663–677.
14. Duro, D.; Franklin, S.; Dube, M. A Comparison of Pixel-Based and Object-Based Image Analysis with Selected Machine Learning Algorithms for the Classification of Agricultural Landscapes Using SPOT-5 HRG Imagery. *Remote Sens. Environ.* **2012**, *118*, 259–272. [[CrossRef](#)]
15. Lin, C.; Wu, C.-C.; Tsogt, K.; Ouyang, Y.-C.; Chang, C.-I. Effects of Atmospheric Correction and Pansharpening on LULC Classification Accuracy Using WorldView-2 Imagery. *Inf. Process. Agric.* **2015**, *2*, 25–36. [[CrossRef](#)]
16. Vapnik, V. *Statistical Learning Theory*; Wiley: New York, NY, USA, 1998.
17. Mountrakis, G.; Im, J.; Ogole, C. Support Vector Machines in Remote Sensing: A Review. *ISPRS J. Photogramm. Remote Sens.* **2011**, *66*, 247–259. [[CrossRef](#)]
18. Postelnik, A. Geometric Potential of Pleiades-1A Satellite Imagery. *GeoSci. Eng.* **2014**, *60*, 19–27. [[CrossRef](#)]
19. Geometric Distortion in Imagery, 2015. Natural Resources Canada. Available online: <http://www.nrcan.gc.ca/node/9401> (accessed on 15 May 2017).
20. Dave, C.P.; Joshi, R.; Srivastava, S. A Survey on Geometric Correction of Satellite Imagery. *Int. J. Comput. Appl.* **2015**, *116*, 24–27.
21. Astrium. *Pleiades Imagery User Guide*; Astrium: Paris, France, 2012.
22. Astrium. *SPOT 6 & SPOT 7 Imagery User Guide*; Astrium: Paris, France, 2013.
23. Chander, G.; Markham, B.; Helder, D. Summary of Current Radiometric Calibration Coefficients for Landsat MSS, TM, ETM+, and EO-1 ALI Sensors. *Remote Sens. Environ.* **2009**, *113*, 893–903. [[CrossRef](#)]
24. Gebreslasie, M.T.; Ahmed, F.B.; van Aardt, J. Image-Based Reflectance Conversion of ASTER and IKONOS Imagery as Precursor to Structural Assessment of Plantation Forests in KwaZulu-Natal, South Africa. *South. For.* **2010**, *71*, 259–265. [[CrossRef](#)]
25. Converting between Julian Dates and Gregorian Calendar Dates, 2016. Astronomical Applications Department of the U.S. Naval Observatory. Available online: <http://aa.usno.navy.mil/data/docs/JulianDate.php> (accessed on 15 May 2017).
26. Zinnert, J.; Shiflett, S.; Via, S.; Bisset, S.; Dows, B.; Manley, P.; Young, D. Spatial-Temporal Dynamics in Barrier Island Upland Vegetation: The Overlooked Coastal Landscape. *Ecosystems* **2016**, *19*, 685–697. [[CrossRef](#)]
27. Moses, W.; Gitelson, A.; Perk, R.; Gurlin, D.; Rundquist, D.; Leavitt, B.; Barrow, T.; Brakhage, P. Estimation of Chlorophyll-a Concentration in Turbid Productive Waters Using Airborne Hyperspectral Data. *Water Res.* **2012**, *46*, 993–1004. [[CrossRef](#)] [[PubMed](#)]
28. Vibhute, A.; Kale, K.; Dhumal, R.; Mehrotra, S. *Hyperspectral Imaging Data Atmospheric Correction Challenges and Solutions Using QUAC and FLAASH Algorithms*; IEEE: Bhubaneswar, India, 2016.

29. Adler-Golden, S.; Bernstein, L.; Matthew, M.; Sundberg, R. Atmospheric Compensation of Extreme Off-Nadir Hyperspectral Imagery from Hyperion. In Proceedings of the SPIE 6565, Algorithms and Technologies for Multispectral, Hyperspectral, and Ultraspectral Imagery XIII, Orlando, FL, USA, 5 July 2007; Volume 65651P.
30. Bernstein, L.; Jin, X.; Gregor, B.; Adler-Golden, S. Quick Atmospheric Correction Code: Algorithm Description and Recent Upgrades. *Opt. Eng.* **2012**, *51*. [[CrossRef](#)]
31. Sun, W.; Chen, B.; Messinger, D. Nearest-Neighbor Diffusion-Based Pan-Sharpening Algorithm for Spectral Images. *Opt. Eng.* **2014**, *53*. [[CrossRef](#)]
32. Jin, X. Segmentation-Based Image Processing System. U.S. Patent No. 8,260,048, 4 September 2012.
33. Robinson, D.; Redding, N.; Crisp, D. *Implementation of a Fast Algorithm for Segmenting SAR Imagery*; DSTO Electronics and Surveillance Research Laboratory: Edinburgh, SA, Australia, 2002.
34. Jensen, J. Thematic Information Extraction: Image Classification. In *Introductory Digital Image Processing: A Remote Sensing Perspective*; Prentice Hall: Upper Saddle River, NJ, USA, 1996; pp. 197–256.
35. Story, M.; Congalton, R. Accuracy Assessment: A User’s Perspective. *Photogramm. Eng. Remote Sens.* **1986**, *52*, 397–399.
36. Olofsson, P.; Foody, G.; Stehman, S.; Woodcock, C. Making Better Use of Accuracy Data in Land Change Studies: Estimate Accuracy and Area and Quantifying Uncertainty Using Stratified Estimation. *Remote Sens. Environ.* **2013**, *129*, 122–131. [[CrossRef](#)]



© 2017 by the authors. Licensee MDPI, Basel, Switzerland. This article is an open access article distributed under the terms and conditions of the Creative Commons Attribution (CC BY) license (<http://creativecommons.org/licenses/by/4.0/>).